NRC Publications Archive
Archives des publications du CNRC

3D Porous Fe/N/C spherical nanostructures as high-performance electrocatalysts for oxygen reduction in both alkaline and acidic media

Wei, Qiliang; Zhang, Gaixia; Yang, Xiaohua; Chenitz, Régis; Banham, Dustin; Yang, Lijun; Ye, Siyu; Knights, Shanna; Sun, Shuhui

NRC Publications Record / Notice d'Archives des publications de CNRC:

https://nrc-publications.canada.ca/eng/view/object/?id=9f231b92-4db5-41e5-a140-4212a5c621f9
https://publications-cnrc.canada.ca/fra/voir/objet/?id=9f231b92-4db5-41e5-a140-4212a5c621f9

Questions? Contact the NRC Publications Archive team at
PublicationsArchive-ArchivesPublications@nrc-cnrc.gc.ca. If you wish to email the authors directly, please see the first page of the publication for their contact information.

Vous avez des questions? Nous pouvons vous aider. Pour communiquer directement avec un auteur, consultez la première page de la revue dans laquelle son article a été publié afin de trouver ses coordonnées. Si vous n'arrivez pas à les repérer, communiquez avec nous à PublicationsArchive-ArchivesPublications@nrc-cnrc.gc.ca.

National Research Council Canada   Conseil national de recherches Canada

Canada

3D Porous Fe/N/C Spherical Nanostructures As High-Performance Electrocatalysts for Oxygen Reduction in Both Alkaline and Acidic Media

Qiliang Wei,[†] Gaixia Zhang,[*,†] Xiaohua Yang,[†] Régis Chenitz,[†] Dustin Banham,[‡] Lijun Yang,[‡] Siyu Ye,[‡] Shanna Knights,[‡] and Shuhui Sun[*,†]

[†]Institut National de la Recherche Scientifique-Énergie Matériaux et Télécommunications, Varennes, Quebec J3X 1S2, Canada
[‡]Ballard Power Systems Inc., Burnaby, British Columbia V5J 5J8, Canada

S Supporting Information

ABSTRACT: Exploring inexpensive and high-performance nonprecious metal catalysts (NPMCs) to replace the rare and expensive Pt-based catalyst for the oxygen reduction reaction (ORR) is crucial for future low-temperature fuel cell devices. Herein, we developed a new type of highly efficient 3D porous Fe/N/C electrocatalyst through a simple pyrolysis approach. Our systematic study revealed that the pyrolysis temperature, the surface area, and the Fe content in the catalysts largely affect the ORR performance of the Fe/N/C catalysts, and the optimized parameters have been identified. The optimized Fe/N/C catalyst, with an interconnected hollow and open structure, exhibits one of the highest ORR activity, stability and selectivity in both alkaline and acidic conditions. In 0.1 M KOH, compared to the commercial Pt/C catalyst, the 3D porous Fe/N/C catalyst exhibits ∼6 times better activity (e.g., 1.91 mA cm^{-2} for Fe/N/C vs 0.32 mA cm^{-2} for Pt/C, at 0.9 V) and excellent stability (e.g., no any decay for Fe/N/C vs 35 mV negative half-wave potential shift for Pt/C, after 10000 cycles test). In 0.5 M H$_2$SO$_4$, this catalyst also exhibits comparable activity and better stability comparing to Pt/C catalyst. More importantly, in both alkaline and acidic media (RRDE environment), the as-synthesized Fe/N/C catalyst shows much better stability and methanol tolerance than those of the state-of-the-art commercial Pt/C catalyst. All these make the 3D porous Fe/N/C nanostructure an excellent candidate for non-precious-metal ORR catalyst in metal−air batteries and fuel cells.

KEYWORDS: nonprecious metal catalyst, 3D, porous, Fe/N/C, oxygen reduction reaction
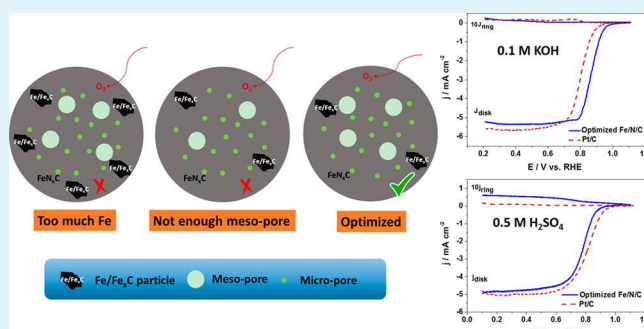
■ INTRODUCTION

Today, the design of inexpensive and highly efficient electrocatalysts for oxygen reduction reaction (ORR) is regarded as a key element for the large-scale application of polymer membrane fuel cells.[1−4] Platinum (Pt) and Pt-based materials are the most effective electrocatalysts for the ORR;[5−7] however, the limited natural reserves and the highly disproportionate geographical distribution of Pt hinder the fuel cell's wide commercialization in the future. Therefore, a wide range of non-Pt-based materials have been actively explored, such as metal-free carbon materials doped with heteroatoms (N, S, B, P),[8−13] metal oxides (Co$_3$O$_4$,[14] Fe$_3$O$_4$,[15] MnO$_2$,[16] etc.) and chalcogenides (Co$_3$S$_4$,[17] FeS$_2$,[18] MnS,[19] etc.) supported on carbon, transition-metal-coordinating macrocyclic compounds,[20,21] and pyrolyzed metal/nitrogen/carbon (M/N/C, M = Fe, Co, Ni) compounds.[22−26] Among them, catalysts based on Fe/N/C are particularly promising, though the exact nature of the active sites (whether the transition metal acts as the activity center or just facilitates the formation of active N−C functional sites)[23,27−31] is still under debate. Nevertheless, it is generally recognized that there are some key factors

governing the ORR activity in the Fe/N/C catalysts: (i) the iron content, (ii) the nitrogen functionalities on the surface, and (iii) the microporous structure.[32,33] Therefore, the careful choice of N and Fe precursors, the carbon support or host for the catalytic sites, as well as the heat-treatment conditions, plays the crucial role in fabricating highly efficient Fe/N/C ORR catalysts. Since their emergence, various Fe and N precursors,[26,27,34−37] and different nanostructures (such as tubes,[22] nanorods,[38] sheets,[39] tetrapods,[40] core−shell structures,[41] porous structure,[37,41] and their hybrids[3,42]) have been designed and reported extensively. Though promising, most of these well-established catalysts can still hardly compete with the overall performance of Pt/C catalyst; in addition, little information is known about the optimal Fe content as well as the microstructures in the Fe/N/C catalysts.

In this work, we explore the use of spherical phenolic resol-F127 monomicelles (SPRMs)[43,44] as the host for impregnating

Scheme 1. Illustration of the Formation of the FexNC-Ar700-NH$_3$-y% Catalysts
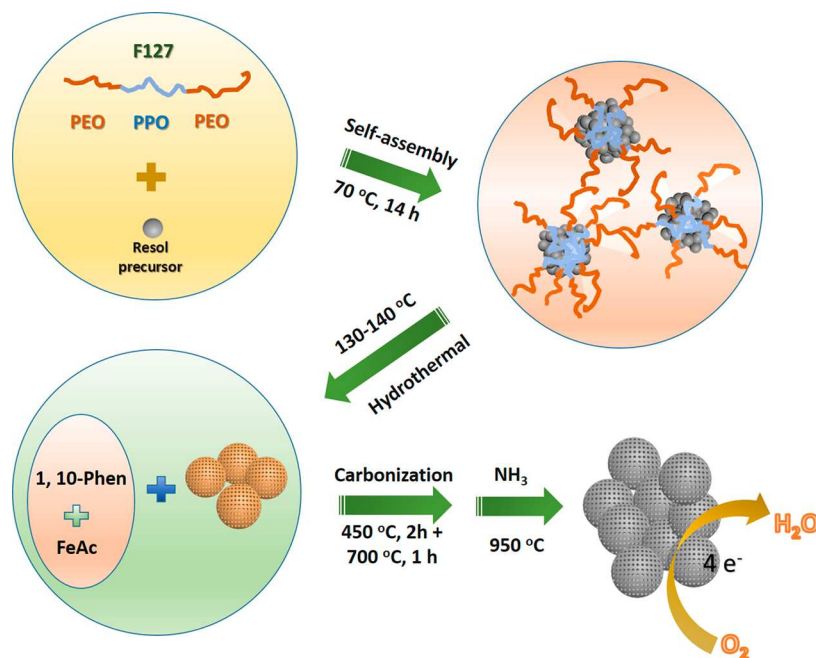
FeAc and 1, 10-Phen to form a catalyst precursor that is subsequently heat treated in Ar and NH$_3$, respectively (Scheme 1). By adjusting the content of FeAc, the pyrolysis temperature in Ar, and pyrolysis time in NH$_3$, a series of Fe/N/C samples (specifically named as FexNC-ArT-NH$_3$-y%, in which, x means the content of FeAc added in the experiment, T means the pyrolysis temperature in Ar, y means the weight remaining after the NH$_3$ pyrolysis, detailed experimental parameters are included in Table S1) were prepared. The content of Fe and surface area of the catalysts can be controllably adjusted by the quantity of FeAc and the pyrolysis time in NH$_3$ atmosphere. Accordingly, the optimized catalyst is obtained showing outstanding ORR activity, stability and methanol crossover tolerance both in alkaline and acidic conditions.

■ EXPERIMENTAL SECTION

Materials. Phenol (99%), formaldehyde solution (37%), iron(II) acetate (95%), 1,10 phenanthroline (99%), sodium hydroxide (NaOH, 95.0%), sulfuric acid (H$_2$SO$_4$, 95.0−98.0%), and potassium hydroxide (KOH, 87.1%), were bought from Fisher Scientific; PluronicF-127, Nafion solution (5 wt %) were purchased from Sigma-Aldrich. All chemicals were used as received and solutions were prepared using deionized water (Millipore Milli-Q, 18.2 MΩ cm).

Preparation of Spherical Phenolic Resol-F127 Monomicelles. First, F127 (0.96 g) was dissolved in 15 mL of DI water at room temperature with stirring for 30 min. Then phenol (0.6 g), formaldehyde solution (2.1 mL), and NaOH aqueous solution (0.1 M, 15 mL) were mixed and stirred at 70 °C for 30 min to obtain a low-molecular-weight phenolic resols. After that, the F127 solution was dropped into the phenolic resols slowly with stirring. Two hours later, 50 mL of water was added and further stirred at 70 °C for 12−14 h. Afterward, 12 mL of the as-prepared monomicelle solution and 25 mL of H$_2$O was transferred into an autoclave (50 mL volume) for hydrothermal treatment at 130 °C for 20 h. In the end, the SPRMs were collected by centrifugation and washed with distilled water for several times, followed by drying in an oven at 60 °C, and then served as the carbon host for loading Fe and N in the next step.

Preparation of Fe/N/C Catalysts. In a typical synthesis of Fe/N/C catalyst, taking Fe30NC-Ar700-NH$_3$-45% as an example, the precursors were prepared by first mixing 700 mg of SPRMs, 136 mg

of 1,10-phenanthroline, and 30 mg of iron(II) acetate in a solution of ethanol and deionized water (ethanol: water = 1:2) under stirring at room temperature. The mixture was then heated to 60−80 °C for 2−3 h until about 50 mL of a thick slurry was obtained. The slurry was placed overnight in a drying oven at 95 °C. Afterward, the dry powder was ground sufficiently and placed in the quartz tube, followed by heating at 450 °C in Ar for 2 h, and then pyrolyzed in Ar at 700 °C for 1 h, followed by another pyrolysis in ammonia at 950 °C with different pyrolysis time in order to obtain expected weight losses. To clarify, all the as-synthesized samples were labeled as FexNC-ArT-NH$_3$-y%, where x is the amount of used FeAc, T is the pyrolysis temperature in Ar (600, 700, and 800 °C), and y is the weight remaining after the NH$_3$ pyrolysis. All information about the amount of precursors, temperatures, pyrolysis durations, and weight remaining of the catalysts after a first pyrolysis in Ar eventually followed by a second pyrolysis in NH$_3$ are summarized in Table S1.

Physical Characterizations. The morphological structures of the catalysts were investigated by transmission electron microscopy (TEM) and high-resolution TEM (HRTEM) (JEOL JEM-2100F, operated at 200 kV). The surface properties were analyzed by X-ray photoelectron spectroscopy (XPS, VG ESCALAB 220i-XL) equipped with a hemispherical analyzer for a Twin Anode X-ray Source. The C 1s peak (BE = 284.6 eV) was used as the reference line to accurately determine the positions of other spectral lines. The fine structure of the photoelectron lines was treated using Casa XPS software (2.3.15 Version). The surface areas of the catalysts were measured through N$_2$ sorption isotherms that were collected using Quantachrome Instruments Autosorb-1 at liquid nitrogen temperature. The surface areas were estimated from the Brunauer−Emmett−Teller (BET) equation and from the fitting of the N$_2$-adsorption isotherms based on a slit-pore model, with the Quenched solid density functional theory (QSDFT) available in the AS1WIN software. The P/P$_0$ range is 0.05− 0.35. QSDFT is an advanced DFT method for the pore size analysis of geometrically and chemically disordered micromesoporous carbons, which allows the calculation of pore size distributions from ca. 0.5 nm up to ca. 40 nm. It allows for a major improvement of the accuracy of DFT pore size distribution analyses of disordered carbon materials from low-temperature nitrogen adsorption isotherms because it takes into account the effects of surface roughness and heterogeneity explicitly.

Electrochemical Measurements. All electrochemical measurements were carried out in a three-electrode cell using a rotating disk
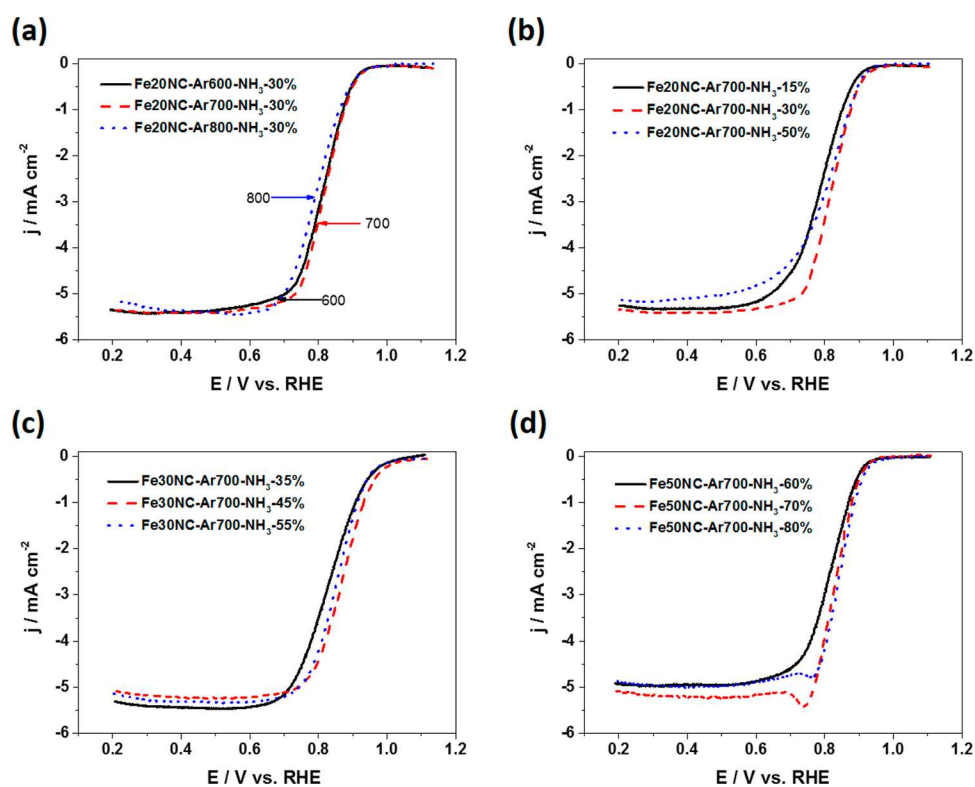
Figure 1. LSV curves of (a) Fe20NC-ArT-NH$_3$-30%, (b) Fe20NC-Ar700-NH$_3$-y%, (c) Fe30NC-Ar700-NH$_3$-y%, (d) Fe50NC-Ar700-NH$_3$-y% in O$_2$-saturated 0.1 M KOH at a scan rate of 10 mV s^{-1}, rotation rate = 1600 rpm.

electrode (RDE, PINE Research Instrumentation) with a bipotentio-stat (Pine, Model PGSTAT-72637) workstation at room temperature. A Pt wire and a saturated calomel electrode (SCE) were used as the counter and reference electrodes, respectively. All potentials in this study refer to reversible hydrogen electrode (RHE). A RDE with glassy carbon (GC) disk electrode (5 mm in diameter) and a rotating ring-disk electrode (RRDE) with a Pt ring and a GC disk (5.61 mm diameter) were used as the substrate for the working electrodes. Before use, the GC electrodes in RDE/RRDE are polished using aqueous alumina suspension on felt polishing pads.

The catalyst suspension in this work was prepared as the following: 10 mg of catalyst was mixed in a glass vial with 95 μL of 5 wt % Nafion solution and 350 μL of ethanol, followed by sonication and agitation in a vortex mixer, alternatively, for a total of 1 h. Then 9 μL of the catalyst suspension was dropped onto the GC electrode surface (~0.8 mg cm^{-2}). For comparison, the 20 wt % Pt/C catalyst (ElectroChem, Inc.) was prepared through the same procedure with a loading amount of 100 μg cm^{-2} (i.e., 20 μg$_{Pt}$ cm^{-2}). Before testing, N$_2$ (or O$_2$) was bubbled through the electrolyte for 30 min and the N$_2$- (or O$_2$) was kept bubbling during the measurements, in order to keep the N$_2$- or O$_2$-saturated solution. In 0.1 M KOH (or 0.5 M H$_2$SO$_4$), the cyclic voltammetry (CV) profiles were recorded at 50 mV s^{-1} and the linear sweep voltammograms (LSV) were recorded at 10 mV s^{-1}, between 0 and 1.2 V (vs RHE). ORR activities were extracted from the negative-going scan for both NPMCs and Pt/C. All of the LSV curves were recorded after subtraction of the background current recorded in N$_2$-saturated solution. For detecting peroxide formed at the disc electrode, the potential for the Pt ring electrode was set at 1.3 V (vs RHE) and the voltammograms were recorded at 1600 rpm. The collection efficiency of the ring-disk electrode was $N = 0.37$. The peroxide yield (H$_2$O$_2$%) and the electron transfer number (n) were calculated as follows:

$$H_2O_2\% = 200(I_r/N)/(I_d + I_r/N)$$

$$n = 4I_d/(I_d + I_r/N)$$

Where I_d is the disk current and I_r is the ring current.

The catalyst tolerance to methanol crossover and the stability were tested in both O$_2$ saturated 0.1 M KOH (or 0.5 M H$_2$SO$_4$) aqueous electrolytes. The methanol crossover effects in CVs were recorded by adding 1.0 M methanol into the electrolytes. The stability test was performed by comparing the LSV curves in O$_2$ saturated electrolytes before and after 2000 cycles with a rotation speed of 1600 rpm. During the cycling test, O$_2$ flow was kept going through the electrolyte to keep the O$_2$-saturated solution.

RESULTS AND DISCUSSION

Previous studies showed that the heat-treatment temperature played a crucial role in the performance of pyrolyzed Fe/N/C catalysts.[26] To investigate the impact of pyrolysis temperature on our catalysts, we first examined the ORR activity of the Fe20NC-ArT-NH$_3$-30% catalysts, as a function of pyrolysis temperature (T) (in the range of 600−800 °C) under Ar, with RRDE measurements performed in 0.1 M KOH electrolyte. As shown in Figure 1a, among these three catalysts, the sample annealed at 700 °C (Fe20NC-Ar700-NH$_3$-30%) displays the highest ORR activity with more positive onset and half-wave potential. This is probably because an optimal balance of electrical conductivity, porosity, and density of active site was achieved at 700 °C.[29,35,45] Accordingly, a series of catalysts (FexNC-Ar700-NH$_3$-y%) discussed below were prepared at 700 °C in the pyrolysis stage of Ar. Then, the content of FeAc (x) and the pyrolysis time in NH$_3$ (y) were adjusted and the ORR activities of the as-synthesized catalysts (FexNC-Ar700-NH$_3$-y%) were investigated systematically by the RRDE measurement in 0.1 M KOH, in order to obtain the optimized x and y for the FexNC-Ar700-NH$_3$-y% samples (Table S1). Specifically, 20, 30, and 50 mg of FeAc was mixed with the same amount of 1,10-Phen and SPRMs, respectively, followed by the same pyrolysis parameter in Ar; then the samples with different quantities (x) of FeAc (Fe20NC-Ar700, Fe30NC-
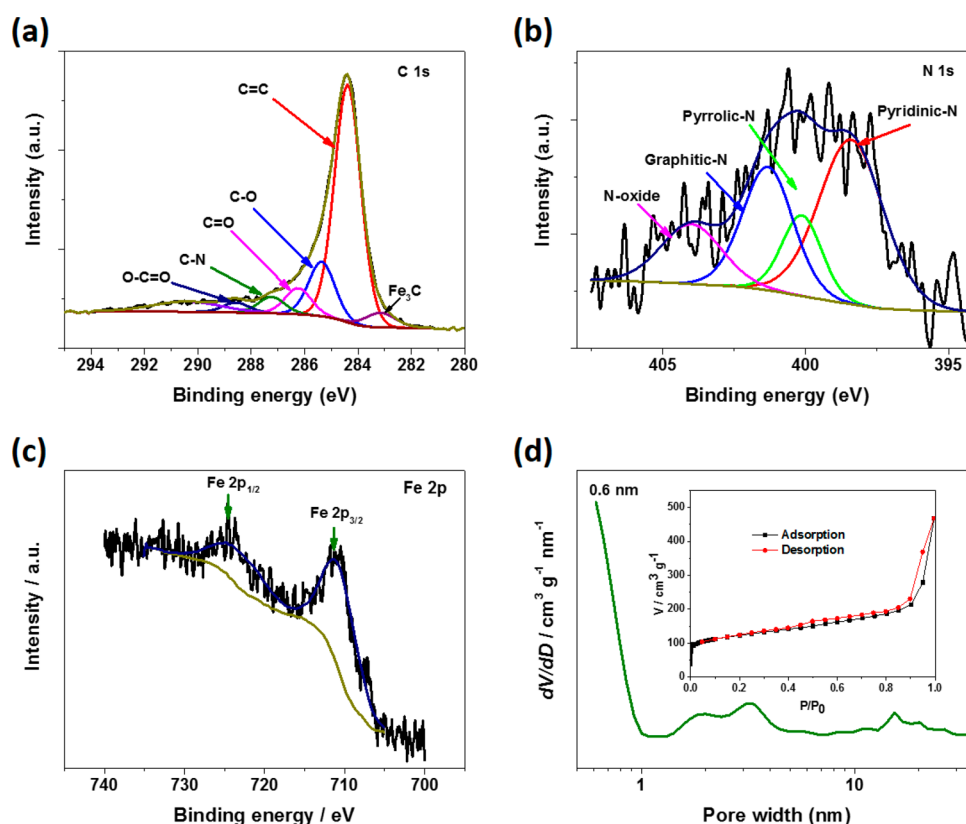
Figure 2. (a) Core level C 1s spectrum, (b) core level N 1s spectrum, (c) core level Fe 2p XPS spectrum of Fe30NC-Ar700-NH$_3$-45%, and (d) pore size distribution of Fe30NC-Ar700-NH$_3$-45%. Inset in Figure 2d is the corresponding N$_2$ isothermal adsorption/desorption curves.

Ar700, and Fe50NC-Ar700) were further annealed under NH$_3$ at 950 °C. For each Fe content group, three different lengths of pyrolysis time under NH$_3$ were preformed, in order to obtain three representative samples with different values of weight remaining (y). In the end, three groups of Fe/N/C samples, named as Fe20NC-Ar700-NH$_3$-y%, Fe30NC-Ar700-NH$_3$-y%, and Fe50NC-Ar700-NH$_3$-y%, were obtained. From the LSV curves for ORR in 0.1 M KOH (Figure 1b-d), samples Fe20NC-Ar700-NH$_3$-30%, Fe30NC-Ar700-NH$_3$-45%, and Fe50NC-Ar700-NH$_3$-80% are proved to be the optimized ones among their corresponding FexNC-Ar700-NH$_3$-y% group samples. Impressively, in 0.1 M KOH, the half-wave potential of ORR on Fe30NC-Ar700-NH$_3$-45% sample reaches 0.87 V (vs RHE). In addition, the Tafel analysis was calculated to further evaluate the ORR kinetic characters of these catalysts. From Figure S1, we can see that the sample Fe30NC-Ar700-NH$_3$-45% has higher current density (1.91 mA cm^{-2}) at 0.9 V with the same catalyst loading on the electrode, comparing to the other samples, which indicates its superior ORR activity. Based on these results, the representative samples, with a focus on the best sample Fe30NC-Ar700-NH3−45%, were selected for the physical characterizations.

The chemical composition of the catalysts was analyzed by XPS. The typical XPS survey spectrum (Figure S2) indicates the existence of Fe, N and C in all FexNC-Ar700-NH$_3$-y% samples. In terms of the presence of oxygen, it probably originates from the SPRM precursors. The C 1s core level XPS spectrum (Figure 2a) of the Fe30NC-Ar700-NH$_3$-45% could be fitted to several different types of C functionalities that correspond to Fe$_3$C, C=C, C−O, C=O, C−N, and O−C= O, respectively, among of which, Fe$_3$C has been demonstrated

to have positive effects for ORR.[46] The high-resolution N 1s XPS spectrum (Figure 2b) of Fe30NC-Ar700-NH$_3$-45% shows that the existence of pyridinic, pyrrolic, and graphitic N and N− O species. It has been demonstrated that the electrocatalytic activity of N-containing catalysts is highly dependent on the pyridinic N content.[42,47−49] Hence, the high proportion of pyridinic N (44.7%) in sample Fe30NC-Ar700-NH$_3$-45% is believed to contribute to the enhanced ORR activity. Two Fe 2p peaks at ∼711 and 725 eV (Figure 2c) corresponding to lower (Fe 2p3/2) and higher (Fe 2p1/2) energies due to spin− orbital splitting were also observed. These results further demonstrate that N and Fe heteroatoms have been doped into the samples, furthermore, the content of Fe measured by XPS (denoted as Fe$_{xps}$) were concluded in Table S2. In addition, it has been reported that all the Fe in the precursor remains in the final catalysts after the pyrolysis,[50] so the Fe concentration can be calculated from the pyrolysis parameters (Table S2), which is denoted as Fe$_{cal}$. Since XPS is a surface-sensitive spectroscopic technique with only several nanometers effective testing depth, it is reasonable that the value of Fe$_{xps}$ is 3−5 times smaller than that of Fe$_{cal}$. Combining the catalytic activities (half-wave potential), it can be concluded that the optimized Fe content (Fe$_{cal}$) in our Fe/N/C catalyst is in the range of 5.5−8 wt % (vs 1.2−2.0% detected by XPS, Fe$_{xps}$). These values are expected to be the reference for similar catalysts in future research.

On the other hand, it has been reported that the large microporous surface area have critical positive influence on the formation of the active sites of Fe and N[27] and mesoporous structure for efficient mass transport, contributing to enhanced ORR activity.[35,40,51] The porous features and the BET specific
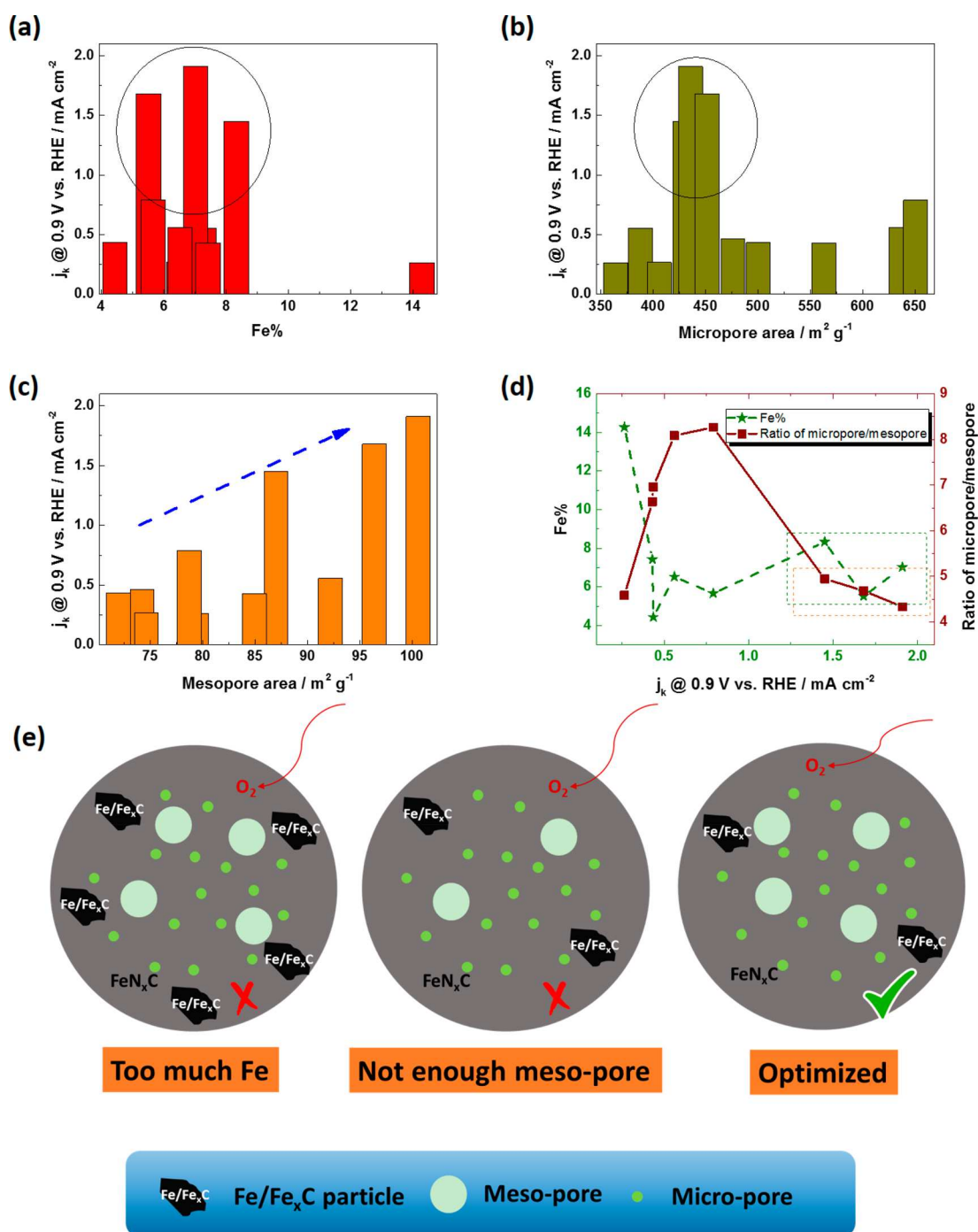
Figure 3. (a) Histogram of j_k@0.9 V with the Fe content in the catalysts, (b, c) histogram of j_k@0.9 V with the micropore surface area and mesopore surface area, and (d) relationships of Fe content, ratio of micropore/mesopore, and j_k@0.9 V. (e) Schematic images of the optimal microstructure of Fe/N/C catalysts.

surface areas of the catalysts were characterized by nitrogen isothermal adsorption/desorption measurements (Figure 2d and Figure S6 and Table S3). They present a sharp uptake at low pressure and a smooth plateau at middle-to-high pressure, which is characteristic of microporous materials. As revealed by the QSDFT pore size distribution (Figure 2d), sample Fe30NC-Ar700-NH$_3$-45% possesses plenty of micropores (around 0.6 nm) and high BET surface area of 536.3 m^2 g^{-1} (with 435.7 m^2 g^{-1} of micropores and 100.6 m^2 g^{-1} of mesopores).

We further investigated the factors which affect the activity of the Fe/N/C catalysts, such as BET surface area (micropores, mesopores, and their ratio), and the Fe content. As shown in Table S3, Figure 3, and Figure S7, it can be seen that (i) the BET surface area (from ~400, ~500, to ~700 m^2 g^{-1}) of the samples increases with the increase of FeAc content (from 20, 30, to 50 mg) in raw materials; (ii) for the samples in the same FeAc content group, the BET surface area decrease with the increase in the Fe amount (Fe$_{cal}$) in the final catalyst, i.e., during NH$_3$ pyrolysis process, the Fe content kept constant, whereas the carbon lost more weight with prolonged pyrolysis time, in

the catalysts;[52] (iii) the optimized Fe% in the final catalysts is in the range of 5.5–8 wt % (Figure 3a); (iv) the optimized micropore surface area is around 450 m^2 g^{-1} (Figure 3b); (v) the activity of our catalyst has increases as the ratio of mesopores increases (Figure 3c), so the optimal ratio of micro/mesopore in these catalysts is around 4–5 (Figure 3d). In summary, the ORR activity can be optimized by the proper balance of Fe content and surface area (microspore and mesopore, as illustrated in Figure 3e). For example, the most active Fe30NC-Ar700-NH$_3$-45% possesses Fe content of 7.02 wt % and the micropore/mesopore ratio of 4.33.

The microstructures of the samples were further characterized by TEM. Figure S3 shows that the carbon host (SPRMs) are spherical with sphere diameter of 50–60 nm and many highly ordered alveoli-like structures. Figure 4 is the
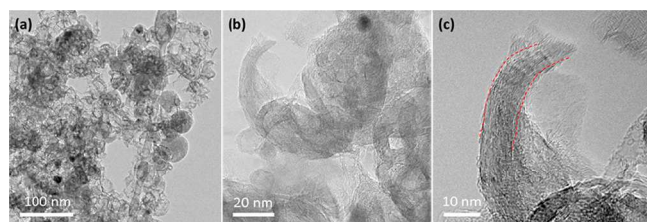

Figure 4. (a–c) TEM images of Fe30NC-Ar700-NH$_3$-45% catalyst at different magnifications.

TEM images of Fe30NC-Ar700-NH$_3$-45% catalyst with different magnifications. The spherical morphology can be mostly preserved even after the high temperature pyrolysis of Ar and NH$_3$, and most of them demonstrated an interconnected

hollow and open structure, having typical wall thickness around 10 nm with 15−20 graphitic layers (Figure 4c), the graphitization nanoshells could enhance the corrosion resistance, thus improve the stability of the catalysts.[25] Besides, it has been reported that ORR can only occur at confined spatial sites, called "triple phase boundaries (TPB)" where electrolyte, gas, and electrically connected catalyst regions contact,[53] therefore, the open and interconnected spherical structure of Fe30NC-Ar700-NH$_3$-45% is expected to offer more active sites for ORR by providing more TPB. While this is not strictly applicable when using RDE which is a two-phase "flooded electrolyte" system, it could provide advantages at the membrane electrode assembly (MEA) level. In addition, the HRTEM image of the black spot in Fe30NC-Ar700-NH3−45% sample (Figure S4) reveals the presence of Fe$_3$C, this carbide may also have synergistic effects with the open and hollow structure in the catalysts to enhance the ORR performance.[46] From Figure S5, it can be seen that the structures for samples of Fe20NC-Ar700-NH$_3$-30% and Fe50NC-Ar700-NH$_3$-80% are similar to that of Fe30NC-Ar700-NH$_3$-45%, whereas the difference lies in that Fe20NC-Ar700-NH$_3$-30% with longer NH$_3$ pyrolysis time shows more irregular morphology, whereas less NH$_3$ pyrolysis time making Fe50NC-Ar700-NH$_3$-80% keeping more regular spherical structure with less open structure.

The electrocatalytic activity, stability, and methanol tolerance of the as-synthesized FexNC-Ar700-NH$_3$-y% catalysts were studied by CV and RRDE techniques. RRDE testing is commonly used for determining the properties of ORR catalysts, in which, both the catalytic activity (from disk measurements) and selectivity to H$_2$O$_2$ formation (from ring measurements) can be directly observed. As shown in Figure 1
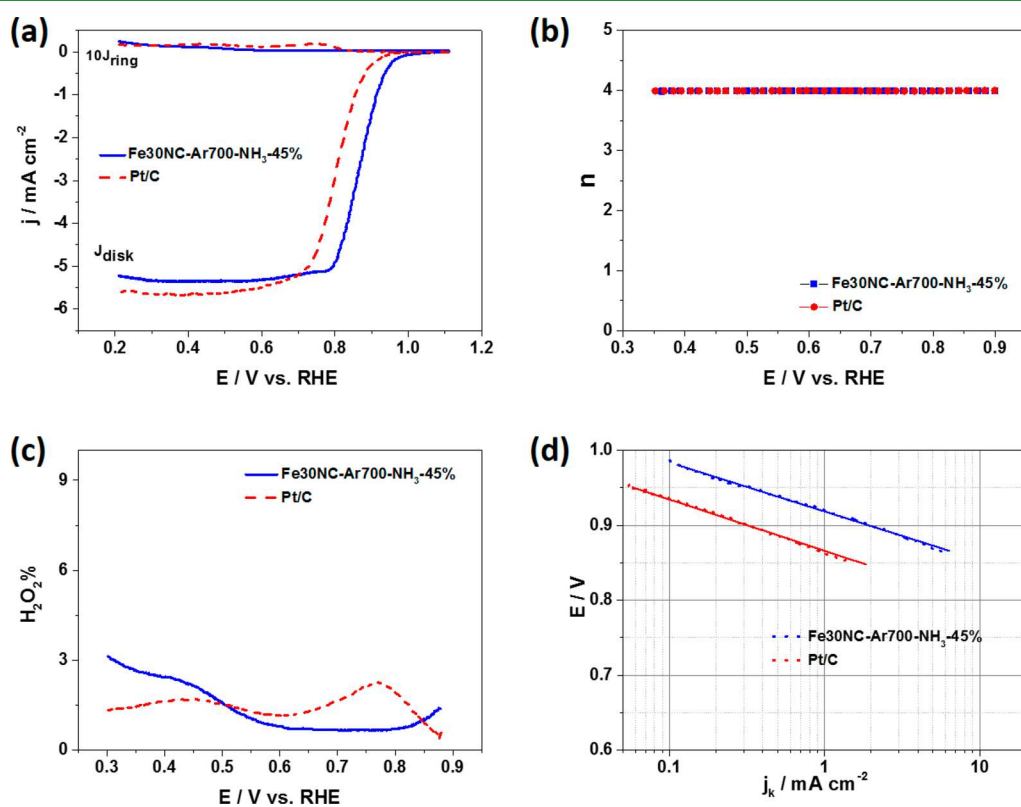

Figure 5. (a) RRDE voltammograms, (b) electron transfer number (*n*), (c) H$_2$O$_2$ yield, (d) Tafel plots of Fe30NC-Ar700-NH$_3$-45% and Pt/C in O$_2$-saturated 0.1 M KOH at a scan rate of 10 mV s^{-1}, rotation rate = 1600 rpm.
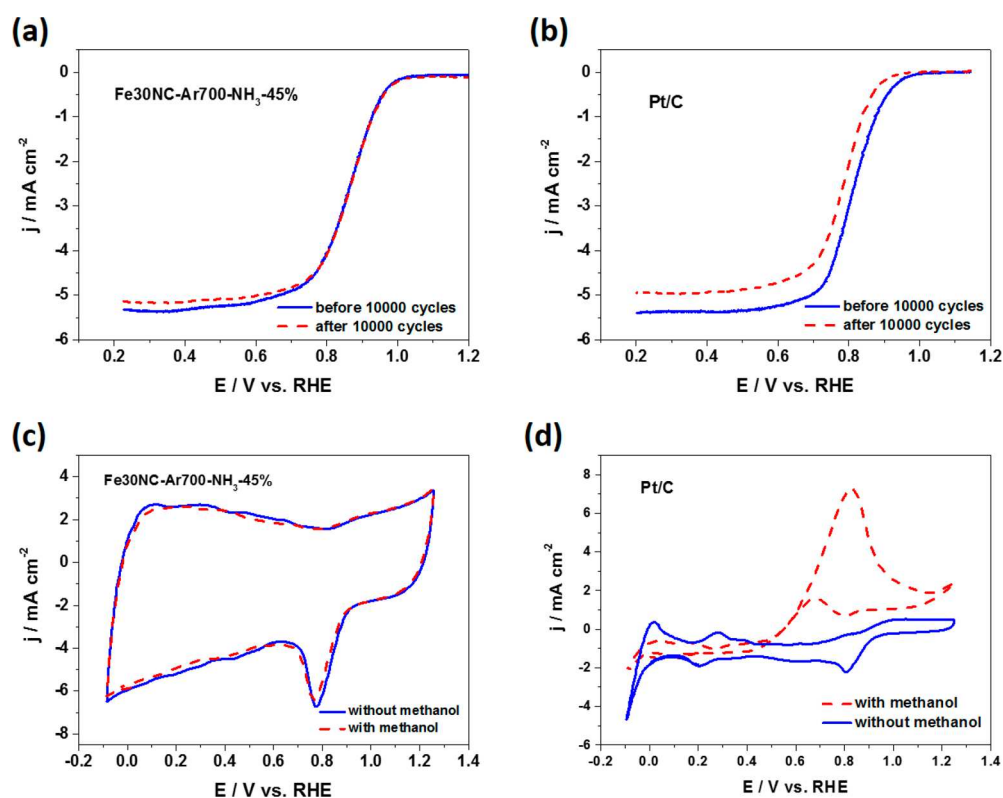
Figure 6. LSV curves of (a) Fe30NC-Ar700-NH$_3$-45% and (b) Pt/C for ORR in O$_2$-saturated 0.1 M KOH before and after 10000 cycles at a scan rate of 200 mV s^{-1} between 0.6 and 1.2 V vs RHE. CV curves of (c) Fe30NC-Ar700-NH$_3$-45% and (d) Pt/C in O$_2$-saturated 0.1 M KOH without and with 1.0 M methanol. Scan rate: 50 mV s^{-1}.
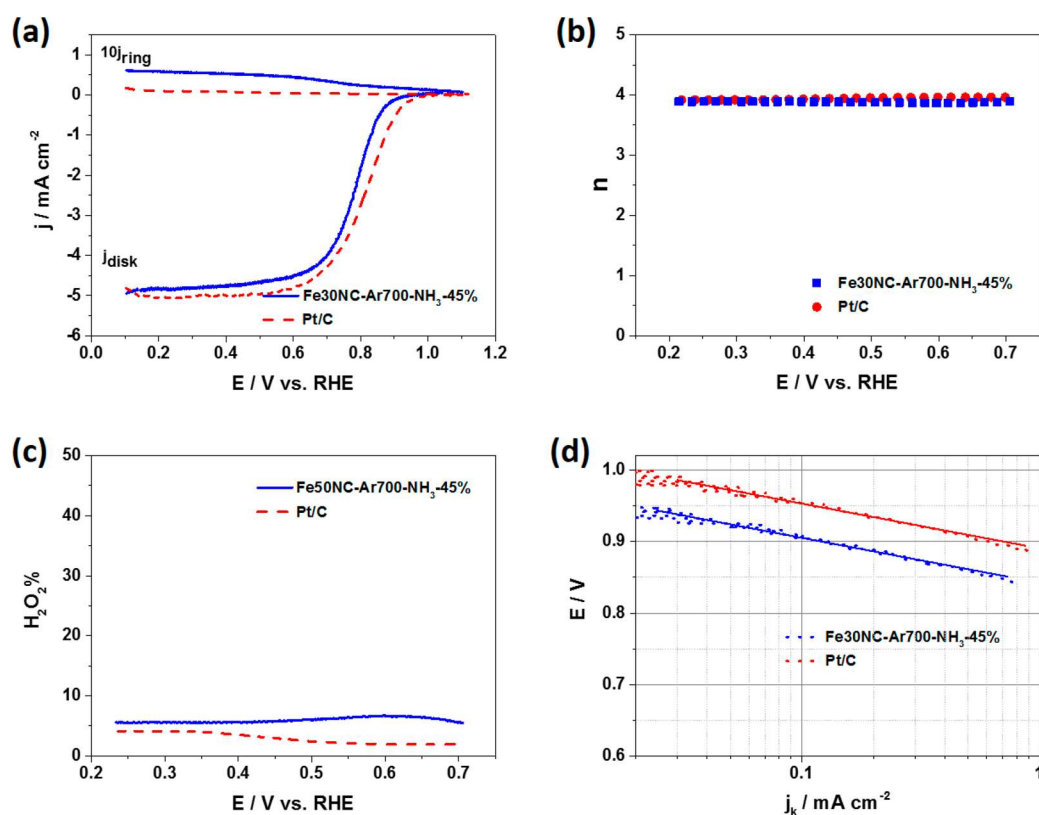

Figure 7. (a) RRDE voltammograms, (b) electron transfer number (n), (c) H$_2$O$_2$ yield, (d) Tafel plots of Fe30NC-Ar-NH$_3$-45% and Pt/C in O$_2$-saturated 0.5 M H$_2$SO$_4$ at a scan rate of 10 mV s^{-1}, rotation rate = 1600 rpm.
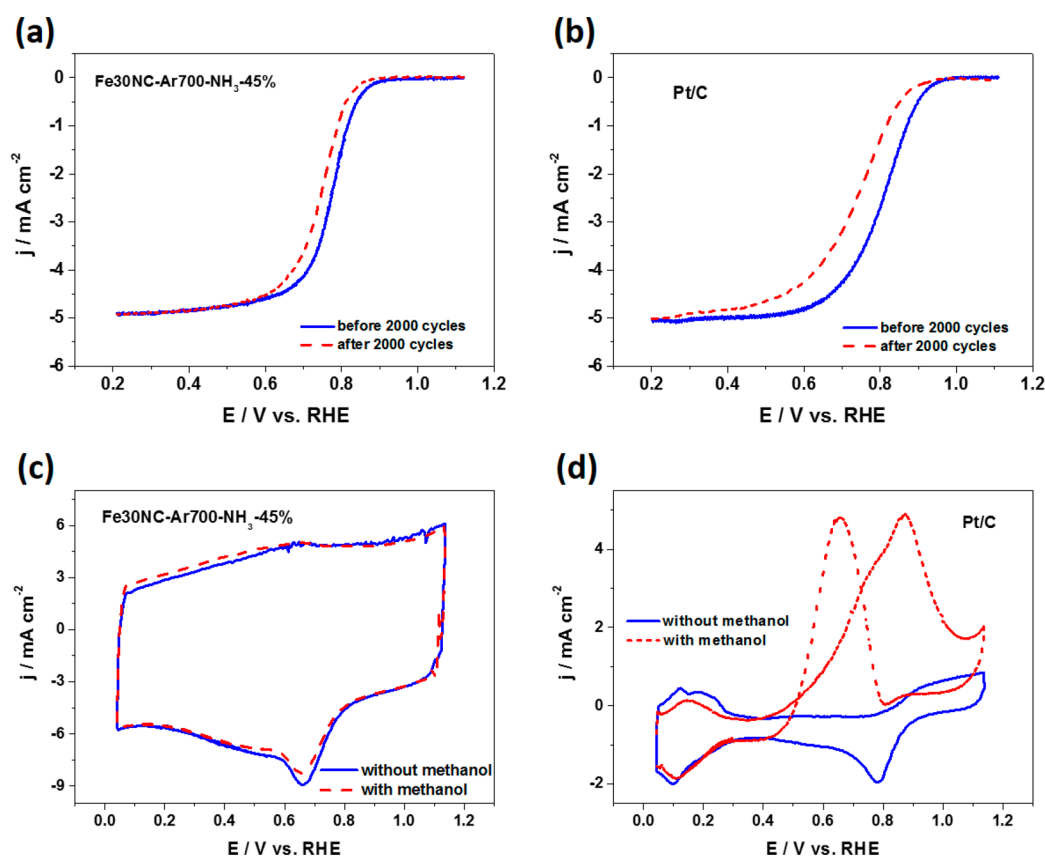
Figure 8. LSV curves of (a) Fe30NC-Ar700-NH$_3$-45% and (b) Pt/C for ORR in O$_2$-saturated 0.5 M H$_2$SO$_4$ before and after 2000 cycles between 0.6 and 1.2 V vs RHE. CV curves of (c) Fe30NC-Ar700-NH$_3$-45% and (d) Pt/C in O$_2$-saturated 0.5 M H$_2$SO$_4$ without and with 1.0 M methanol. Scan rate: 50 mV s^{-1}.

and Figure S1, by comparing the LSV curves and Tafel plot in 0.1 M KOH, relative to other FexNC-Ar700-NH$_3$-y% catalysts, Fe30NC-Ar700-NH$_3$-45% displays a superior ORR activity with more positive half-wave potential and onset potential (E_{onset}), as well as higher activity at 0.9 V (vs RHE). Figure 5a shows the typical RRDE voltammograms of Fe30NC-Ar700-NH$_3$-45% and commercial Pt/C catalyst obtained at room temperature in O$_2$-saturated 0.1 M KOH solution. It can be seen that the current density at 0.85 V can be achieved 3.43 mA cm^{-2} for Fe30NC-Ar700-NH$_3$-45% vs 1.15 mA cm^{-2} for Pt/C (with higher loading for NPMC). RRDE test results show that Fe30NC-Ar700-NH$_3$-45% has a high electron-transfer number of 3.98, almost the same as that of the Pt/C catalyst. Moreover, the H$_2$O$_2$ yield measured with the Fe30NC-Ar700-NH$_3$-45% catalyst remained below 3% at all potentials in 0.1 M KOH. More impressively, in the range of 0.5−0.85 V (vs RHE), the H$_2$O$_2$ yielding of Fe30NC-Ar700-NH$_3$-45% is below 1.5%, even lower than that of commercial Pt/C. This negligible H$_2$O$_2$ yield clearly confirms that Fe30NC-Ar700-NH$_3$-45% has extremely high ORR catalytic efficiency. Figure 5d shows the Tafel plots of Fe30NC-Ar700-NH$_3$-45% and commercial Pt/C, derived from Figure 5a. In the low overpotential region, Fe30NC-Ar700-NH$_3$-45% has a Tafel slope of 67 mV/decade in 0.1 M KOH, close to the 66 mV/decade of the Pt/C, indicating that the rate-determining step for the ORR occurring at Fe30NC-Ar700-NH$_3$-45% is similar to that of Pt.

Moreover, benefiting from the graphitized carbon phase (Figure 4c), Fe30NC-Ar700-NH$_3$-45% shows outstanding stability for ORR in alkaline media, as confirmed by the absence of an ORR polarization curve shift after 10 000 cycles

between 0.6 to 1.2 V (Figure 6a), whereas there was a 35 mV negative shift of half-wave potential for the Pt/C catalyst under the same conditions (Figure 6b), suggesting that under RRDE experiment, Fe30NC-Ar700-NH$_3$-45% is more stable than Pt/C. Furthermore, for the application of direct methanol fuel cells (DMFC), the methanol on the anode side could go through membrane to the cathode side, leading to a "mixed potential effect", which would severely deteriorate the ORR performance, therefore, the methanol tolerance of the Fe30NC-Ar700-NH$_3$-45% and Pt/C catalysts was evaluated by adding 1.0 M methanol into 0.1 M KOH electrolyte. After addition of methanol, there is almost no change in the ORR peak current for Fe30NC-Ar700-NH$_3$-45% (Figure 6c); however, the typical inverse methanol oxidation peaks in CVs were observed (Figure 6d) for the Pt/C catalyst. These results suggest that Fe30NC-Ar700-NH$_3$-45% has much better methanol tolerance (i.e., catalytic selectivity toward ORR) than the commercial Pt/C catalyst in alkaline media.

Importantly, Fe30NC-Ar700-NH$_3$-45% catalyst is also active and stable for ORR in acidic media. As shown in Figure 7a, in 0.5 M H$_2$SO$_4$ electrolyte, Fe30NC-Ar700-NH$_3$-45% shows slightly negative shift (∼30 mV), in terms of the on-set potential and half-wave potential, compared with those of Pt/C. The transferred electron number per O$_2$ molecule for Fe30NC-Ar700-NH$_3$-45% and Pt/C electrodes in the acidic medium is 3.89 and 3.93 (Figure 7b), respectively, suggesting a nearly 4e$^-$ ORR pathway even in the acidic solution. The calculated yields of H$_2$O$_2$ for the Fe30NC-Ar700-NH$_3$-45% and Pt/C electrodes are less than 6.5% and 4.1% respectively, under the potential range of 0.2−0.7 V (Figure 7c). Figure 7d shows the Tafel plots

of Fe30NC-Ar700-NH$_3$-45% and commercial Pt/C, derived from Figure 7a. The Tafel slope of both Fe30NC-Ar700-NH$_3$-45% and the Pt/C are around 62 mV/decade, indicating that Fe30NC-Ar700-NH$_3$-45% also has the similar reaction mechanism of ORR as commercial Pt/C in the low overpotential area.

The stability test was also carried out under the identical conditions. From Figure 8a, d, it can be seen that Fe30NC-Ar700-NH$_3$-45% sample shows better ORR stability than the Pt/C catalyst, as indicated by a much lower polarization curve shift (25 vs 65 mV for Pt/C), after 2000 cycles' tests. From the methanol crossover test, we can see that in the presence of 1.0 M methanol, there is only a slight change of peak current for Fe30NC-Ar700-NH$_3$-45% (Figure 8c), whereas significant methanol oxidation peaks in CVs for the Pt/C catalyst (Figure 8d) can be observed, suggesting that Fe30NC-Ar700-NH$_3$-45% also has excellent selectivity for ORR with strong tolerance to methanol crossover effect in acidic media.

CONCLUSIONS

To sum up, a series of 3D microporous Fe/N/C ORR catalysts were prepared by employing SPRMs as the carbon host for impregnating FeAc and 1, 10-Phen, followed by high temperature pyrolysis in Ar in NH$_3$ atmosphere, consequently. Through the systematic studies, we found that (i) the content of Fe precursor and pyrolysis time under NH$_3$ have distinct influence to the morphology and structure of the final Fe/N/C catalysts; (ii) the pyrolysis temperature in Ar, the BET surface area, and the content of Fe in the catalysts largely affect the ORR activity; (iii) the optimized Fe content of the Fe/N/C catalysts is around 5.5−8 wt % and the optimized porosity is with 450 m^2 g^{-1} micropore with preferably higher value of mesopores, only catalysts subjecting within these two ranges exhibit high activity. The Fe30NC-Ar700-NH$_3$-45% catalyst shows an interconnected hollow and open spherical structure with optimized Fe content (∼7 wt %), BET surface area (536.3 m^2 g^{-1}, with 435.7 m^2 g^{-1} of micropores and 100.6 m^2 g^{-1} of mesopores with a Rmicro/meso of 4.33), and exhibits good ORR performances in both alkaline and acidic conditions. In alkaline solution, it shows a half-wave potential of 0.87 V, excellent stability even in O$_2$-saturated solution, and strong methanol tolerance. Moreover, in acidic solution, Fe30NC-Ar700-NH$_3$-45% also exhibits excellent stability and selectivity. Notably, the ORR process of Fe30NC-Ar700-NH$_3$-45% catalyst in both alkaline and acidic media follows the direct 4e$^-$ transfer pathway, indicating a complete reduction of O$_2$ to water. All these characters make our Fe/N/C catalyst a very good non-noble-metal candidate for ORR. This work provides more insights to fabricate highly efficient Fe/N/C catalysts in both acidic and alkaline electrolytes, which may boost the development of various fuel cells.

ASSOCIATED CONTENT

Ⓢ Supporting Information

The Supporting Information is available free of charge on the ACS Publications website at DOI: 10.1021/acsami.7b12666.

> Tafel plots in O$_2$-saturated 0.1 M KOH; XPS spectra; TEM and HRTEM images; N$_2$ isothermal adsorption/desorption curves; relationships of micropore, mesopore, and Fe content with the current density j_k@0.9 V; experimental parameters during the preparation of FexNC-ArT-NH$_3$-y% samples, relationship of the cata-

lytic activity and the Fe, N content (wt %); N$_2$ adsorption/desorption analysis (PDF)

AUTHOR INFORMATION

Corresponding Authors
*E-mail: gaixia.zhang@emt.inrs.ca.
*E-mail: shuhui@emt.inrs.ca.

ORCID Ⓞ
Siyu Ye: 0000-0002-4384-5025
Shuhui Sun: 0000-0002-0508-2944

Author Contributions
The manuscript was written through contributions of all authors. All authors have given approval to the final version of the manuscript.

Notes
The authors declare no competing financial interest.

REFERENCES

(1) Peng, Z.; Freunberger, S. A.; Hardwick, L. J.; Chen, Y.; Giordani, V.; Bardé, F.; Novák, P.; Graham, D.; Tarascon, J. M.; Bruce, P. G. Oxygen Reactions in a Non−Aqueous Li$^+$ Electrolyte. *Angew. Chem.* **2011**, *123* (28), 6475−6479.

(2) Steele, B. C. H.; Heinzel, A. Materials for Fuel-Cell Technologies. *Nature* **2001**, *414* (6861), 345−352.

(3) Liang, J.; Zhou, R. F.; Chen, X. M.; Tang, Y. H.; Qiao, S. Z. Fe−N Decorated Hybrids of CNTs Grown on Hierarchically Porous Carbon for High−Performance Oxygen Reduction. *Adv. Mater.* **2014**, *26* (35), 6074−6079.

(4) Shao, M.; Chang, Q.; Dodelet, J.-P.; Chenitz, R. Recent Advances in Electrocatalysts for Oxygen Reduction Reaction. *Chem. Rev.* **2016**, *116* (6), 3594−3657.

(5) Sun, S.; Zhang, G.; Geng, D.; Chen, Y.; Li, R.; Cai, M.; Sun, X. A Highly Durable Platinum Nanocatalyst for Proton Exchange Membrane Fuel Cells: Multiarmed Starlike Nanowire Single Crystal. *Angew. Chem.* **2011**, *123* (2), 442−446.

(6) Sun, S.; Jaouen, F.; Dodelet, J. P. Controlled Growth of Pt Nanowires on Carbon Nanospheres and Their Enhanced Performance as Electrocatalysts in PEM Fuel Cells. *Adv. Mater.* **2008**, *20* (20), 3900−3904.

(7) Bing, Y.; Liu, H.; Zhang, L.; Ghosh, D.; Zhang, J. Nanostructured Pt-Alloy Electrocatalysts for PEM Fuel Cell Oxygen Reduction Reaction. *Chem. Soc. Rev.* **2010**, *39* (6), 2184−2202.

(8) Chen, L.; Chen, Z.; Huang, Z.; Huang, Z.; Wang, Y.; Li, H.; Zhou, H.; Kuang, Y. Influence of Carbon Precursors on the Structure, Composition and Oxygen Reduction Reaction Performance of Nitrogen-Doped Carbon Materials. *J. Phys. Chem. C* **2015**, *119* (52), 28757−28765.

(9) Jiang, W.-J.; Hu, J.-S.; Zhang, X.; Jiang, Y.; Yu, B.-B.; Wei, Z.-D.; Wan, L.-J. In Situ Nitrogen-Doped Nanoporous Carbon Nanocables as An Efficient Metal-Free Catalyst for Oxygen Reduction Reaction. *J. Mater. Chem. A* **2014**, *2* (26), 10154−10160.

(10) Wei, Q.; Tong, X.; Zhang, G.; Qiao, J.; Gong, Q.; Sun, S. Nitrogen-Doped Carbon Nanotube and Graphene Materials for Oxygen Reduction Reactions. *Catalysts* **2015**, *5* (3), 1574−1602.

(11) Ma, Z.; Dou, S.; Shen, A.; Tao, L.; Dai, L.; Wang, S. Sulfur–Doped Graphene Derived from Cycled Lithium–Sulfur Batteries as a Metal–Free Electrocatalyst for the Oxygen Reduction Reaction. *Angew. Chem.* **2015**, *127* (6), 1908–1912.

(12) Gong, Y.; Fei, H.; Zou, X.; Zhou, W.; Yang, S.; Ye, G.; Liu, Z.; Peng, Z.; Lou, J.; Vajtai, R. Boron-and Nitrogen–Substituted Graphene Nanoribbons as Efficient Catalysts for Oxygen Reduction Reaction. *Chem. Mater.* **2015**, *27* (4), 1181–1186.

(13) Zhang, C.; Mahmood, N.; Yin, H.; Liu, F.; Hou, Y. Synthesis of Phosphorus–Doped Graphene and Its Multifunctional Applications for Oxygen Reduction Reaction and Lithium Ion Batteries. *Adv. Mater.* **2013**, *25* (35), 4932–4937.

(14) Liang, Y.; Li, Y.; Wang, H.; Zhou, J.; Wang, J.; Regier, T.; Dai, H. Co_3O_4 Nanocrystals On Graphene as A Synergistic Catalyst for Oxygen Reduction Reaction. *Nat. Mater.* **2011**, *10* (10), 780–786.

(15) Wu, Z.-S.; Yang, S.; Sun, Y.; Parvez, K.; Feng, X.; Müllen, K. 3D Nitrogen–Doped Graphene Aerogel-Supported Fe_3O_4 Nanoparticles as Efficient Electrocatalysts for The Oxygen Reduction Reaction. *J. Am. Chem. Soc.* **2012**, *134* (22), 9082–9085.

(16) Cheng, F.; Su, Y.; Liang, J.; Tao, Z.; Chen, J. MnO_2-Based Nanostructures as Catalysts for Electrochemical Oxygen Reduction in Alkaline Media†. *Chem. Mater.* **2010**, *22* (3), 898–905.

(17) Mahmood, N.; Zhang, C.; Jiang, J.; Liu, F.; Hou, Y. Multifunctional Co_3S_4/Graphene Composites for Lithium Ion Batteries and Oxygen Reduction Reaction. *Chem. - Eur. J.* **2013**, *19* (16), 5183–5190.

(18) Susac, D.; Zhu, L.; Teo, M.; Sode, A.; Wong, K. C.; Wong, P. C.; Parsons, R. R.; Bizzotto, D.; Mitchell, K. A. R.; Campbell, S. A. Characterization of FeS_2-Based Thin Films as Model Catalysts for the Oxygen Reduction Reaction. *J. Phys. Chem. C* **2007**, *111* (50), 18715–18723.

(19) Liu, X.; Du, J.; Li, C.; Han, X.; Hu, X.; Cheng, F.; Chen, J. The Anion Effect on the Oxygen Reduction of MnX (X= O, S, and Se) Catalysts. *J. Mater. Chem. A* **2015**, *3* (7), 3425–3431.

(20) Cao, R.; Thapa, R.; Kim, H.; Xu, X.; Kim, M. G.; Li, Q.; Park, N.; Liu, M.; Cho, J. Promotion of Oxygen Reduction by a Bio-Inspired Tethered Iron Phthalocyanine Carbon Nanotube-based Catalyst. *Nat. Commun.* **2013**, *4*, 2076.

(21) Wei, P. J.; Yu, G. Q.; Naruta, Y.; Liu, J. G. Covalent Grafting of Carbon Nanotubes with a Biomimetic Heme Model Compound to Enhance Oxygen Reduction Reactions. *Angew. Chem., Int. Ed.* **2014**, *53* (26), 6659–6663.

(22) Chung, H. T.; Won, J. H.; Zelenay, P. Active and Stable Carbon Nanotube/Nanoparticle Composite Electrocatalyst for Oxygen Reduction. *Nat. Commun.* **2013**, *4*, 1922.

(23) Lin, L.; Zhu, Q.; Xu, A.-W. Noble-Metal-Free Fe–N/C Catalyst for Highly Efficient Oxygen Reduction Reaction under Both Alkaline and Acidic Conditions. *J. Am. Chem. Soc.* **2014**, *136* (31), 11027–11033.

(24) Liu, J.; Sun, X.; Song, P.; Zhang, Y.; Xing, W.; Xu, W. High–Performance Oxygen Reduction Electrocatalysts based on Cheap Carbon Black, Nitrogen, and Trace Iron. *Adv. Mater.* **2013**, *25* (47), 6879–6883.

(25) Wu, G.; More, K. L.; Johnston, C. M.; Zelenay, P. High-Performance Electrocatalysts for Oxygen Reduction Derived from Polyaniline, Iron, and Cobalt. *Science* **2011**, *332* (6028), 443–447.

(26) Wu, Z. Y.; Xu, X. X.; Hu, B. C.; Liang, H. W.; Lin, Y.; Chen, L. F.; Yu, S. H. Iron Carbide Nanoparticles Encapsulated in Mesoporous Fe–N–Doped Carbon Nanofibers for Efficient Electrocatalysis. *Angew. Chem.* **2015**, *127* (28), 8297–8301.

(27) Lefèvre, M.; Proietti, E.; Jaouen, F.; Dodelet, J.-P. Iron–based Catalysts with Improved Oxygen Reduction Activity in Polymer Electrolyte Fuel Cells. *Science* **2009**, *324* (5923), 71–74.

(28) Wu, G.; Chen, Z.; Artyushkova, K.; Garzon, F. H.; Zelenay, P. Polyaniline-Derived Non-Precious Catalyst for the Polymer Electrolyte Fuel Cell Cathode. *ECS Trans.* **2008**, *16* (2), 159–170.

(29) Ferrandon, M.; Kropf, A. J.; Myers, D. J.; Artyushkova, K.; Kramm, U.; Bogdanoff, P.; Wu, G.; Johnston, C. M.; Zelenay, P. Multitechnique Characterization of A Polyaniline–Iron–Carbon Oxygen Reduction Catalyst. *J. Phys. Chem. C* **2012**, *116* (30), 16001–16013.

(30) Wu, G.; Johnston, C. M.; Mack, N. H.; Artyushkova, K.; Ferrandon, M.; Nelson, M.; Lezama-Pacheco, J. S.; Conradson, S. D.; More, K. L.; Myers, D. J.; Zelenay, P. Synthesis–Structure–Performance Correlation for Polyaniline–Me–C Non-Precious Metal Cathode Catalysts for Oxygen Reduction in Fuel Cells. *J. Mater. Chem.* **2011**, *21* (30), 11392–11405.

(31) Zhu, Y.; Zhang, B.; Liu, X.; Wang, D. W.; Su, D. S. Unravelling the Structure of Electrocatalytically Active Fe–N Complexes in Carbon for the Oxygen Reduction Reaction. *Angew. Chem., Int. Ed.* **2014**, *53* (40), 10673–10677.

(32) Kramm, U. I.; Herranz, J.; Larouche, N.; Arruda, T. M.; Lefèvre, M.; Jaouen, F.; Bogdanoff, P.; Fiechter, S.; Abs-Wurmbach, I.; Mukerjee, S.; Dodelet, J.-P. Structure of the Catalytic Sites in Fe/N/C-Catalysts for O_2-Reduction in PEM Fuel Cells. *Phys. Chem. Chem. Phys.* **2012**, *14* (33), 11673–11688.

(33) Jaouen, F.; Lefèvre, M.; Dodelet, J.-P.; Cai, M. Heat-Treated Fe/N/C Catalysts for O_2 Electroreduction: Are Active Sites Hosted in Micropores? *J. Phys. Chem. B* **2006**, *110* (11), 5553–5558.

(34) Wang, M.-Q.; Yang, W.-H.; Wang, H.-H.; Chen, C.; Zhou, Z.-Y.; Sun, S.-G. Pyrolyzed Fe–N–C Composite As an Efficient Non-Precious Metal Catalyst for Oxygen Reduction Reaction in Acidic Medium. *ACS Catal.* **2014**, *4* (11), 3928–3936.

(35) Liang, H.-W.; Wei, W.; Wu, Z.-S.; Feng, X.; Müllen, K. Mesoporous Metal–Nitrogen-Doped Carbon Electrocatalysts for Highly Efficient Oxygen Reduction Reaction. *J. Am. Chem. Soc.* **2013**, *135* (43), 16002–16005.

(36) Kramm, U. I.; Herrmann-Geppert, I.; Fiechter, S.; Zehl, G.; Zizak, I.; Dorbandt, I.; Schmeißer, D.; Bogdanoff, P. Effect of Iron-Carbide Formation on the Number of Active Sites in Fe–N–C Catalysts for the Oxygen Reduction Reaction in Acidic Media. *J. Mater. Chem. A* **2014**, *2* (8), 2663–2670.

(37) Su, Y.; Jiang, H.; Zhu, Y.; Zou, W.; Yang, X.; Chen, J.; Li, C. Hierarchical Porous Iron and Nitrogen Co-Doped Carbons as Efficient Oxygen Reduction Electrocatalysts in Neutral Media. *J. Power Sources* **2014**, *265*, 246–253.

(38) Wen, Z.; Ci, S.; Zhang, F.; Feng, X.; Cui, S.; Mao, S.; Luo, S.; He, Z.; Chen, J. Nitrogen–Enriched Core–Shell Structured Fe/Fe_3C–C Nanorods as Advanced Electrocatalysts for Oxygen Reduction Reaction. *Adv. Mater.* **2012**, *24* (11), 1399–1404.

(39) Xiang, Z.; Xue, Y.; Cao, D.; Huang, L.; Chen, J. F.; Dai, L. Highly Efficient Electrocatalysts for Oxygen Reduction Based on 2D Covalent Organic Polymers Complexed with Non–precious Metals. *Angew. Chem., Int. Ed.* **2014**, *53* (9), 2433–2437.

(40) Lee, J. S.; Park, G. S.; Kim, S. T.; Liu, M.; Cho, J. A Highly Efficient Electrocatalyst for the Oxygen Reduction Reaction: N–Doped Ketjenblack Incorporated into Fe/Fe_3C–Functionalized Melamine Foam. *Angew. Chem.* **2013**, *125* (3), 1060–1064.

(41) Zhou, M.; Yang, C.; Chan, K. Y. Structuring Porous Iron–Nitrogen–Doped Carbon in a Core/Shell Geometry for the Oxygen Reduction Reaction. *Adv. Energy Mater.* **2014**, *4* (18), 1400840.

(42) Yang, W.; Liu, X.; Yue, X.; Jia, J.; Guo, S. Bamboo-like Carbon Nanotube/Fe_3C Nanoparticle Hybrids and Their Highly Efficient Catalysis for Oxygen Reduction. *J. Am. Chem. Soc.* **2015**, *137* (4), 1436–1439.

(43) Fang, Y.; Gu, D.; Zou, Y.; Wu, Z.; Li, F.; Che, R.; Deng, Y.; Tu, B.; Zhao, D. A Low–Concentration Hydrothermal Synthesis of Biocompatible Ordered Mesoporous Carbon Nanospheres with Tunable and Uniform Size. *Angew. Chem., Int. Ed.* **2010**, *49* (43), 7987–7991.

(44) Wei, Q.; Fu, Y.; Zhang, G.; Wang, Y.; Wang, X.; Mohamedi, M.; Sun, S. Highly-Ordered Microporous Carbon Nanospheres: A Promising Anode for High-Performance Sodium-Ion Batteries. *RSC Adv.* **2016**, *6* (87), 84149–84154.

(45) Wei, J.; Liang, Y.; Zhang, X.; Simon, G. P.; Zhao, D.; Zhang, J.; Jiang, S.; Wang, H. Controllable Synthesis of Mesoporous Carbon Nanospheres and Fe–N/Carbon Nanospheres As Efficient Oxygen Reduction Electrocatalysts. *Nanoscale* **2015**, *7* (14), 6247–6254.

(46) Hu, Y.; Jensen, J. O.; Zhang, W.; Cleemann, L. N.; Xing, W.; Bjerrum, N. J.; Li, Q. Hollow Spheres of Iron Carbide Nanoparticles Encased in Graphitic Layers As Oxygen Reduction Catalysts. *Angew. Chem., Int. Ed.* **2014**, *53* (14), 3675−3679.

(47) Rao, C. V.; Cabrera, C. R.; Ishikawa, Y. In Search of the Active Site in Nitrogen-Doped Carbon Nanotube Electrodes for the Oxygen Reduction Reaction. *J. Phys. Chem. Lett.* **2010**, *1* (18), 2622−2627.

(48) Xing, T.; Zheng, Y.; Li, L. H.; Cowie, B. C. C.; Gunzelmann, D.; Qiao, S. Z.; Huang, S.; Chen, Y. Observation of Active Sites for Oxygen Reduction Reaction on Nitrogen-Doped Multilayer Graphene. *ACS Nano* **2014**, *8* (7), 6856−6862.

(49) Guo, D.; Shibuya, R.; Akiba, C.; Saji, S.; Kondo, T.; Nakamura, J. Active Sites of Nitrogen-Doped Carbon Materials for Oxygen Reduction Reaction Clarified Using Model Catalysts. *Science* **2016**, *351* (6271), 361−365.

(50) Yang, L.; Larouche, N.; Chenitz, R.; Zhang, G.; Lefèvre, M.; Dodelet, J.-P. Activity, Performance, and Durability for the Reduction of Oxygen in PEM Fuel Cells, of Fe/N/C Electrocatalysts Obtained from the Pyrolysis of Metal-Organic-Framework and Iron Porphyrin Precursors. *Electrochim. Acta* **2015**, *159*, 184−197.

(51) Wang, H.; Ishihara, S.; Ariga, K.; Yamauchi, Y. All-Metal Layer-By-Layer Films: Bimetallic Alternate Layers with Accessible Mesopores for Enhanced Electrocatalysis. *J. Am. Chem. Soc.* **2012**, *134* (26), 10819−10821.

(52) Zhang, G.; Chenitz, R.; Lefèvre, M.; Sun, S.; Dodelet, J.-P. Is Iron Involved in the Lack of Stability of Fe/N/C Electrocatalysts Used to Reduce Oxygen at the Cathode of PEM Fuel Cells? *Nano Energy* **2016**, *29*, 111−125.

(53) O'Hayre, R.; Barnett, D. M.; Prinz, F. B. The Triple Phase Boundary A Mathematical Model and Experimental Investigations for Fuel Cells. *J. Electrochem. Soc.* **2005**, *152* (2), A439−A444.